Ultracold neutral plasma expansion in a strong uniform magnetic field

R. Tucker Sprenkle, S. D. Bergeson, Luciano G. Silvestri, and Michael S. Murillo

Phys. Rev. E **105**, 045201 — Published 6 April 2022
DOI: 10.1103/PhysRevE.105.045201

Ultracold neutral plasma expansion in a strong uniform magnetic field

R. Tucker Sprenkle* and S. D. Bergeson†
Department of Physics and Astronomy
Brigham Young University, Provo, UT 84602, USA

Luciano G. Silvestri and Michael S. Murillo
Department of Computational Mathematics, Science and Engineering
Michigan State University, East Lansing, MI 48824, USA
(Dated: February 16, 2022)

In strongly magnetized neutral plasmas, electron motion is reduced perpendicular to the magnetic field direction. This changes dynamical plasma properties such as temperature equilibration, spatial density evolution, electron pressure, and thermal and electrical conductivity. In this paper we report measurements of free plasma expansion in the presence of a strong magnetic field. We image laser-induced fluorescence from an ultracold neutral Ca^+ plasma to map the plasma size as a function of time for a range of magnetic field strengths. The asymptotic expansion velocity perpendicular to the magnetic field direction falls rapidly with increasing magnetic field strength. We observe that the initially Gaussian spatial distribution remains Gaussian throughout the expansion in both the parallel and perpendicular directions. We compare these observations with a diffusion model and with a self-similar expansion model and show that neither of these models reproduces the observed behavior over the entire range of magnetic fields used in this study. Modeling the expansion of a magnetized ultracold plasma poses a nontrivial theoretical challenge.

I. INTRODUCTION

Ultracold neutral plasmas (UNPs) are useful tools in understanding transport properties of strongly coupled systems. They provide an idealized platform for measuring plasma transport properties [1–5] and can simulate high energy-density plasmas (HEDPs) over a limited range of conditions [2, 6–15]. The high optical opacity and short dynamic time scales in HEDPs pose challenges to experimentally measuring transport properties with high fidelity. For this reason interpretations of HEDP measurements rely heavily on molecular dynamics (MD) simulations [16] and plasma models [17, 18] to understand transport in these complex systems. UNPs have the advantage of low density (10^7 to 10^{13} cm^{-3}) and low temperature (0.05 to 2 K), resulting in accessible real-time measurements of plasma properties [2, 3, 19, 20] in the strongly-coupled plasma regime. Transport properties measured in this idealized environment can be used to verify plasma models and MD simulations [9, 21–25].

Transport properties in magnetized plasmas continues to be a significant research area in the plasma physics community [26–36], including studies of UNPs [37–41]. Recent work in UNP magnetic confinement opens an exciting new avenue of magnetized plasma transport research [42].

In this work we present UNP expansion measurements in the presence of a strong, uniform magnetic field. Using circularly polarized state-selective laser induced fluorescence, we measure the plasma size as a function of time and deduce the asymptotic expansion rate. This work extends previous measurements reported in Ref. 37 to greater magnetic field strengths. We compare our results to a diffusion model [37] and show that it fails to reproduce our measured expansion rates. We also consider a self-similar expansion model [43]. While this model matches the zero-field results, it fails to reproduce the magnetized plasma measurements. Modeling the expansion of magnetized plasmas poses a nontrivial theoretical challenge. UNPs provide a platform for measuring possible theories with high accuracy.

The degree of magnetization for species s can be parameterized using the ratio,

$$\alpha_s = \frac{\Omega_{cs}}{\nu_{si}} \tag{1}$$

where $\Omega_{cs} = eB/m_s$ is the cyclotron frequency of species s, mass m_s, in magnetic field B, and ν_{si} is the species-ion collision frequency [44]. When $\alpha_s > 1$, the species is magnetized, meaning that the collision dynamics are significantly changed by the magnetic field.

We explore Ca^+ UNP expansion with the applied field strength ranging from $B = 0$ to 0.12 T. The electron magnetization parameter spans from zero to $\alpha_e = 350$. The ions are always unmagnetized. At the highest field values, the ion cyclotron frequency is $\Omega_{ci} = 3 \times 10^5$ s^{-1}, $\nu_{ii} = 1 \times 10^7$ [45], making $\alpha_i \leq 0.03$.

In this paper we measure the transverse and parallel expansion of our Ca^+ UNP and compare the experimental data to an ambipolar diffusion model [37] and a self-similar expansion model. We show that neither of these reproduces the experimental data over the entire range of magnetic field strengths.

---

* Quantinuum, 303 S Technology Ct, Broomfield, CO 80021, USA
† scott.bergeson@byu.edu

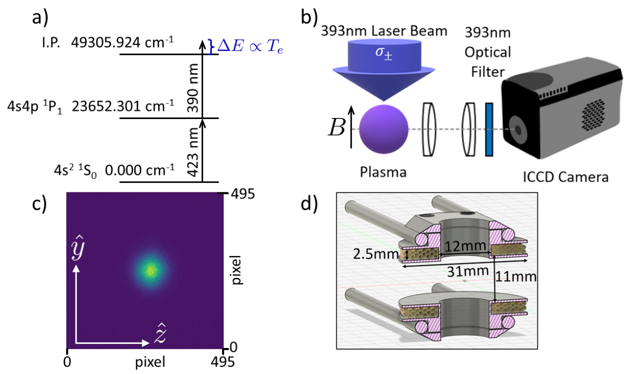

FIG. 1. Experimental details. a) Partial energy level diagram for Ca showing ionization laser wavelengths. I.P. = Ionization Potential. b) A circularly polarized 393 nm probe laser beam illuminates the UNP. Fluorescence photons are collected by a 1:1 optical relay system, optically filtered, and imaged onto an ICCD camera. c) Frequency-integrated UNP fluorescence image when $B = 0$ and $t = 0$. The $\hat{y}$ and $\hat{z}$ directions are labeled. The image is 496×496 pixels, with a pixel spacing of 13.0 μm per pixel, making the image size 6.4×6.4 mm. d) Cross-sectional view of magnetic field coils and mounting hardware. The coils are centered on the UNP.

II. EXPRIMENTAL DETAILS

Working at somewhat lower density, approximately 3 million neutral Ca atoms are trapped in a magnet-optical trap (MOT) using 423 nm laser beams [9, 25]. The Ca$^+$ plasma is formed by ionizing 80% of the Ca atoms by two color resonant photoionization using 5 ns laser pulses at 423 nm and 390 nm, as shown in Fig. 1a. The photon energy of the 390 nm laser above the ionization limit controls the electron temperature, T_e. In this work $T_e =$ 96 K to effectively eliminate three-body recombination.

The Ca$^+$ plasma is observed using laser-induced fluorescence. The entire plasma is illuminated by a 393 nm circularly-polarized probe laser beam driving the Ca$^+$ 393 nm $4s\ ^2S_{1/2} \rightarrow 4p\ ^2P_{3/2}$ transition. The RMS width of the probe laser beam is 1620 ± 90 μm. The fluorescence from the plasma is optically filtered and imaged onto a image-intensified CCD (ICCD) camera using a 1:1 imaging system, see Fig. 1b. Plasma fluorescence is measured with the probe laser frequency set to 11 different offset frequencies relative to the atomic resonance, ranging from ±200 MHz in 40 MHz steps. The sum of these images provides a side-on view of the plasma, as shown in Fig. 1c.

The plasma density is calculated by combining measurements of both the neutral atoms and the plasma ions. We use resonant absorption imaging of the neutral atom cloud to determine the density, rms width, and number of atoms in the MOT. We determine the ionization fraction by measuring MOT fluorescence before and after the ionizing laser pulses. We allow the neutral atom cloud to expand before ionization to reduce the density relative to the MOT and to smooth out any local density variations.

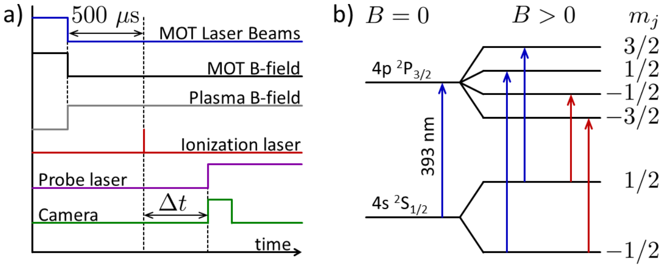

FIG. 2. Timing schematic and partial energy level diagram. a) Timing sequence for the experiment. The MOT fields turn off and the neutral atom cloud begins expanding slightly 500 μs before the ionizing laser pulses form the plasma. During this time interval, a uniform field with B ranging up to 0.12 T turns on. b) Zeeman splitting of the $4s\ ^2S_{1/2} - 4p\ ^2P_{3/2}$ transition. Because the laser beam propagates along the magnetic field direction, only $\Delta m = \pm 1$ transitions are allowed. The $m_{\mathrm{lower}} = \pm 1/2 \rightarrow m_{\mathrm{upper}} = \pm 3/2$ transitions shift at $\Delta f/B = 13.99$ GHz/T. The $m_{\mathrm{lower}} = \pm 1/2 \rightarrow m_{\mathrm{upper}} = \mp 1/2$ transitions shift at $\Delta f/B = 23.35$ GHz/T.

Using the MOT density, the ionization fraction, the rms MOT width, and the initial plasma rms width, we calculate the plasma density. The initial plasma spatial density distribution is Gaussian and spherically symmetric, $n(r) = n_0 \exp\left(-r^2/2\sigma_0^2\right)$, with $\sigma_0 = 400 \pm 20$ μm and $n_0 = 3.4 \pm 0.2\ \times 10^{15}$ m^{-3}. The ion temperature is set by disorder-induced heating to be approximately 2 K [9].

A constant uniform magnetic field is made using electrical coils separated by 11 mm inside the vacuum chamber in a near-Helmholtz configuration. The magnetic field strengths used in this paper are $B = 0, 0.005, 0.011, 0.020, 0.051,$ and 0.123T. The magnetic field direction defines the $\hat{z}$ direction in Fig. 1c. The coils are wrapped onto a stainless steel spool mounted to the optical imaging system, as shown in Fig. 1d. The spool is cut to eliminate eddy currents when the magnetic field changes. The stainless steel housing is grounded to suppress electric fields arising from the potential difference between the coils. Currents ranging up to 150 A are supplied to the coils to produce magnetic field strengths up to 0.12 T.

The current in the coils turns on 500 μs prior to ionization to allow the magnetic field to approach a steady state value. During this time the MOT laser beams and MOT magnetic field are turned off and the neutral atom cloud freely expands. The neutral atom cloud expansion is not influenced by the applied magnetic field. Once the atoms are ionized the magnetic field remains on for ≈ 50 μs before turning off. This is repeated at a rate of 10 Hz. Timing details are shown in Fig. 2a.

III. ZEEMAN SHIFTS

The magnetic field splits the $4s\ ^2S_{1/2} \rightarrow 4p\ ^2P_{3/2}$ transition into several Zeeman components, as shown in Fig.

2b. The linear Zeeman shift is calculated as,

$$\Delta E = \mu_B g_L m_j B \tag{2}$$

where μ_B is the Bohr magneton, $g_L = 1.333861(25)$ and $g_L = 2.00225664(9)$ are the Landé g-factors for the ${}^2P_{3/2}$ and ${}^2S_{1/2}$ levels, respectively [46–48], and m_j is the magnetic angular momentum quantum number.

Zeeman splitting of the excited and ground states of Ca$^+$ opens pathways to several optically dark states. To eliminate the dark ground state, the probe laser beam propagates along the magnetic field direction. It is circularly polarized and selections rules only allow $\Delta m = \pm 1$ transitions. This prevents optical pumping into the ${}^2S_{1/2}(m = -1/2)$ state. There is a small probability after excitation that ions in the ${}^2P_{3/2}(m_j = 3/2)$ state will decay into optically dark D states. In our previous work, these dark states were optically pumped back into the excited states to allow for long measurement times [2, 9]. With a magnetic field, repumping is less practical because there are 5 optically allowed transitions into the ${}^2D_{5/2}$ and ${}^2D_{3/2}$ Zeeman states. Rather than optically pumping out these dark states, the probe laser is turned on at some time Δt after plasma formation and observed by the ICCD camera for only 100-200 ns, as shown in Fig. 2c. The finite pulse width contributes approximately 1.5 MHz to the observed linewidth of the 393 nm transition. Because we integrate over frequency to determine the areal density, this additional width is negligible.

IV. IMAGE DATA REDUCTION AND ANALYSIS

The ICCD camera records a spatially resolved fluorescence image at a specific time after the plasma is formed. For a specific frequency of the probe laser, the fluorescence intensity in the camera is proportional to the number of ions Doppler- and Zeeman-shifted into resonance with the probe laser beam at a particular point in space and time. The Doppler shift arises from both the ion thermal velocity and the plasma hydrodynamic expansion velocity.

Camera images are recorded at 11 laser frequencies at times $t = 0.1$, 1, 2, 5, 10, 20 μs for each magnetic field strength. We process these images to extract the rms size of the plasma transverse and parallel to the magnetic field. From this data the asymptotic expansion velocity is calculated in both the parallel and perpendicular directions.

A. Analysis of $\sigma_{\parallel}$

Summing the 11 camera images at a particular time and magnetic field strength create a projection of the spatial density distribution onto the yz plane, as shown in Fig. 1c. At late times, as the hydrodynamic velocity increases, the Doppler shift at large $\pm z$ exceeds the probe laser detuning frequency. Therefore the late-time images only explore the central regions of the plasma along the magnetic field direction, $\hat{z}$.

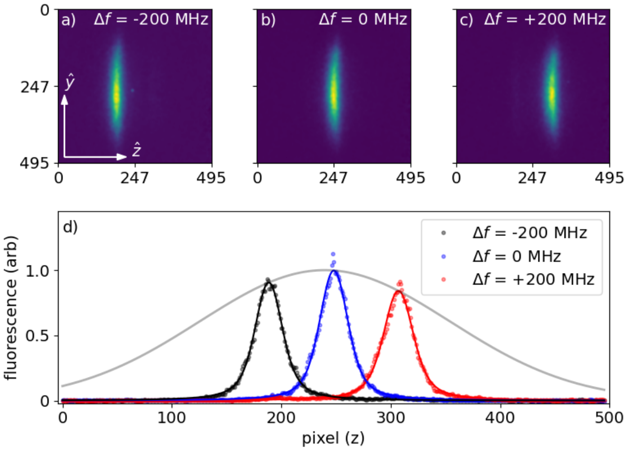

FIG. 3. Fluorescence images and $\sigma_{\parallel}$ analysis for $B = 0$ at a delay time of 10 μs. Panels a), b), and c) show fluorescence images for three different values of the probe laser frequency detuning, as indicated in the panels. The images are integrated along the y direction and plotted in panel d). Circles show the measured data. The solid black, blue, and red lines show Voigt fits to the data. The fitted peak amplitude and pixel locations are used to fit the Gaussian envelope (shown as a gray solid line). Eight additional measurements are not shown, for clarity.

The analysis for plasma expansion in the z-direction for $\sigma_{\parallel}$ is illustrated in Fig. 3, for $B = 0$, and Fig. 4, for $B = 0.020$ T. In a plasma image recorded with the probe laser frequency fixed at a particular value, the z-axis in the image can be mapped onto the plasma hydrodynamic expansion velocity. For a self-similar expansion, applicable when $B = 0$, the mapping is 1:1. The z-axis is directly proportional to hydrodynamic velocity through the Doppler shift. In Fig. 3a-c, the fluorescence images for three different probe laser detunings are shown at a delay time of $\Delta t = 10$ μs after the plasma is formed when $B = 0$. As the probe laser frequency changes, the location of the fluorescence also changes. Ions that are Doppler-shifted into resonance with the probe laser frequency scatter photons most strongly. Voigt profile fits to the integrated fluorescence signal are plotted in black, blue, and red in Fig. 3d. We fit the corresponding peak locations and amplitudes to a Gaussian envelope profile to determine the rms width of the plasma in the z-direction.

When the magnetic field is present, the fluorescence measurements are consistent with a self-similar plasma expansion along the magnetic field direction, just as in the $B = 0$ case. In Fig. 4 fluorescence images for three different probe laser detunings are shown at a delay time

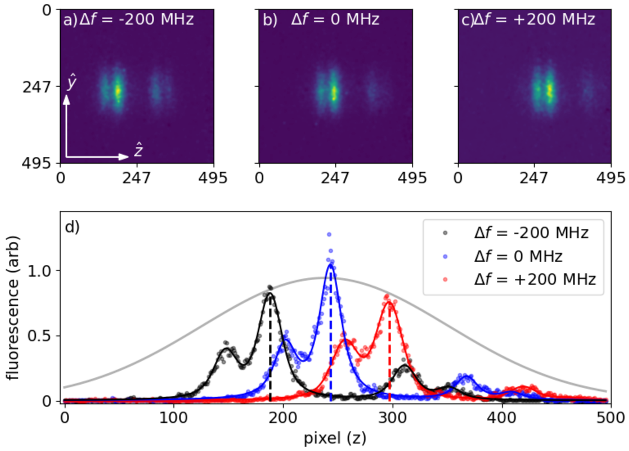

FIG. 4. Fluorescence images and $\sigma_\parallel$ analysis for $B = 0.020$ T at a delay time of 10 μs. Panels a), b), and c) show fluorescence images for three different values of the probe laser frequency detuning, as indicated in the panels. The horizontal and vertical axes are pixel number in the images. The images are integrated along the y direction and plotted in panel d). The four Zeeman transitions indicated in Fig. 1c) are clearly visible. Also shown in d) are lineshape fits as described in the text. The vertical dashed lines show the locations of the $\frac{1}{2} \rightarrow \frac{3}{2}$ transitions used to fit the Gaussian envelope. The rms width of this envelope is $\sigma_\parallel$, and it is plotted in Fig. 5. The gray solid line is the expected Gaussian envelope from the hydrodynamic model at 10 μs. Eight additional measurements are not shown, for clarity.

of 10 μs after the plasma is formed when $B = 0.020$ T. Four transitions are clearly visible, indicating that our probe laser polarization is not purely σ^+ polarized. These correspond to the $m_{\text{lower}} - m_{\text{upper}}$ transitions $1/2 \rightarrow 3/2$, $-1/2 \rightarrow 1/2$, $1/2 \rightarrow -1/2$, and $-1/2 \rightarrow -3/2$ shown in Fig. 2b. Correspondingly, we fit these images to the sum of four Voigt profiles with the amplitudes, center frequencies, and widths as fit parameters. We constrain the relative separation between peaks to be consistent with Eq. (2) and the known Lande-g factors, assuming a linear mapping of the hydrodynamic velocity onto the z-axis. We also constrain the Lorentzian and Gaussian widths to be the same for all peaks in the fit. As shown in Fig. 4d, the fits are in excellent agreement with the data. The number of Zeeman components used in the fits, and the number visible in the line shapes, depends on both the value of the magnetic field strength and the delay time. We note that this analysis only probes the central region of the plasma. It seems likely that near the edges of the plasma, as the density falls, the plasma description becomes kinetic.

Finally, in Fig. 5 we show the rms width of the plasma as a function of time for several different magnetic field strengths. The data at 5, 10, and 20 μs are slightly offset in the plot to better illustrate the data and associated estimated error bars. Although there is some scatter in the measurements, these data suggest that the expansion in the magnetic field direction is self-similar. This is perhaps expected, as the magnetic field does not exert any forces in the z-direction.

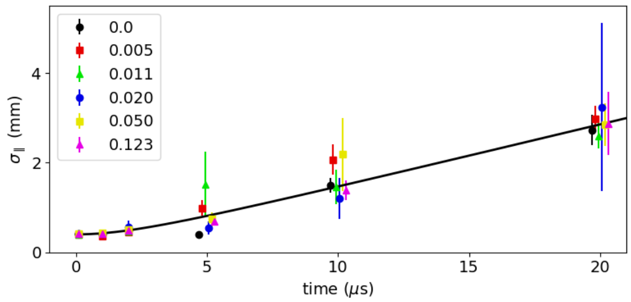

FIG. 5. Time-evolution of the plasma envelope along the z-direction. The points show the measured Gaussian envelope rms width, $\sigma_\parallel$, as described in the text. The values of the magnetic field strength in Tesla is indicated in the legend. The solid black line shows the expected rms width using the measured initial plasma parameters $\sigma_0 = 0.4$ mm and $T_{e0} = 96$ K. The values at 5, 10, and 20 μs are slightly offset in time to better show the data. These data suggest that the plasma expanion in the z-direction, parallel to the magnetic field, is Gaussian and self-similar because it agrees with a hydrodynamic model near the plasma center.

B. Analysis of $\sigma_\perp$

The rms width of the plasma in the y-direction, $\sigma_\perp(t)$, is determined by summing the fluorescence images over all laser detunings and then integrating along the z-direction. The fluorescence signals are corrected slightly for the Gaussian profile of the probe laser beam along the y-direction by dividing the integrated fluorescence profiles by a Gaussian with an rms width of 1.62 ± 0.09 mm.

To model the data, we considered four different lineshapes: Lorentzian, Voigt, Gaussian, and super-Gaussian of order 4. These data and model fits are shown in Fig. 6. The super-Gaussian (red line) and Lorentzian (blue line) models are poor representations of the data. When considering the entire data set, the Voigt (green line) and Gaussian (magenta line) profiles are nearly indistinguishable. Based on this analysis, the Gaussian appears to be the best model for all cases. This suggests a self-similar Gaussian expansion in the perpendicular direction, consistent with the Gaussian transverse expansion data reported in Ref. [37]. This observation suggests that we use a hydrodynamic model to interpret the perpendicular expansion data.

The measured rms widths of the plasmas as a function of time for different magnetic field strengths is shown in the left panel of Fig. 7. The expansion data are fit to a

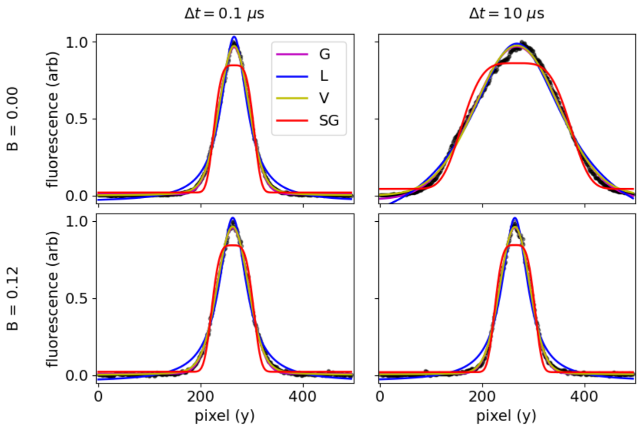

FIG. 6. Model selection for $\sigma_\perp(t)$. Plots of the projections of the fluorescence signals along the y-axis for different delay times and magnetic field strengths. The black dots show the data. The magenta line shows a Gaussian fit. The blue line shows a Lorentzian fit. The yellow line shows a Voigt fit. The red line shows a super-Gaussian fit of order 4. The Gaussian and Voigt fits are indistinguishable in nearly all cases.

hydrodynamic model,

$$\sigma_\perp(t, B) = \sigma_0 \left[1 + \left(\frac{t}{\tau(B)}\right)^2\right]^{1/2}, \tag{3}$$

with σ_0 and $\tau(B)$ as fit parameters. In an unmagnetized $B = 0$ hydrodynamic UNP model, the expansion time is $\tau^2 = (m_i\sigma_0)/(k_B T_{e0})$ [49]. However, in our model when $B \neq 0$, τ is only phenomenological. It merely parameterizes the plasma expansion in the perpendicular direction. The expansion curves derived from Eq. (3) are shown as solid lines in Fig. 7a, and reproduce the data well. The fitted values of σ_0 and τ are given in Table I. At late times, when $t \gg \tau$, $\sigma(t) \approx (\sigma_0/\tau)t$ and the asymptotic expansion velocity is

$$v_{\text{exp}} \equiv \sigma_0/\tau(B). \tag{4}$$

In the opposite limit, when $t \ll \tau$, $\sigma(t) \approx \sigma_0[1 + t^2/(2\tau^2)]$.

We next explore the functional dependence of v_{exp} on B. To do this, we fit v_{exp} to three different models, each of which has two parameters. The best model is selected visually by evaluating its representation of the data. The three models are an exponential form,

$$v_{\text{exp}} = a \exp(-B/b), \tag{5}$$

and a power-law form,

$$v_{\text{exp}} = a(b + B)^{-p}. \tag{6}$$

The values of a and b are least-squares fit parameters. The power-laws we explore are $p = \frac{1}{2}$ and 1. The $p = \frac{1}{2}$ model was suggested in Ref. [37]. In Eq. (6) we have added an offset parameter b relative to Ref. [37] to allow the model to cover the entire range of B, including the $B = 0$ data.

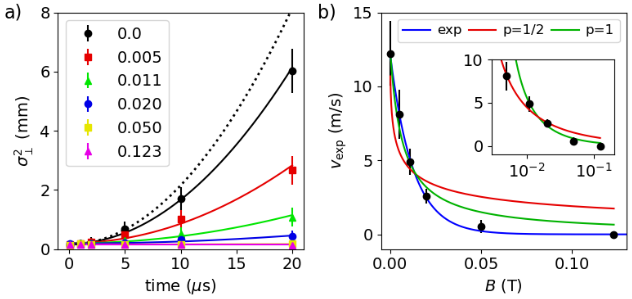

FIG. 7. Analysis of $\sigma_\perp$. a) Plots of $\sigma_\perp^2(t)$ for different values of the magnetic field. The magnetic field strength in Tesla is indicated in the legend. The points are the fitted rms widths $\sigma_\perp(t, B)$ using Eq. (3). The vertical lines indicate the estimated systematic uncertainty associated with the finite Gaussian width of the probe laser beam. If the expansions were diffusive, the squared widths would increase linearly in time. b) $v_{\text{exp}} = \sigma_0/\tau(B)$ plotted vs. B (black points). Also plotted are model fits to the data as described in the text. Inset: Semilogarithmic plots of power-law fits [Eq. (6)] to subsets of the data, as explained in the text. The exponential fit is the best representation of the entire data set. The power laws fit well in different limits.

TABLE I. Values of the fit parameters σ_0 and $\tau(B)$ obtained by fitting the data in Fig. 7a to Eq. (3). The numbers in parenthesis following the numbers in the table are the estimated statistical uncertainties in the last digits. For the $B = 0.123$ T data, the least squares fitting routine cannot estimate the uncertainty in τ.

B	σ_0 (mm)	$\tau(B)$ μs
0.000	0.42(3)	3.5(3)
0.005	0.45(4)	5.5(6)
0.011	0.45(2)	9.1(8)
0.020	0.44(2)	17(2)
0.050	0.40(1)	74(60)
0.123	0.40(1)	6E4

The model that best represents the entire data set is the exponential fit,

$$v_{\text{exp}} = (12.1 \text{ mm}/\mu\text{s}) \exp[-B/(0.013 \text{ T})]. \tag{7}$$

The coefficient 12.1 mm/μs is equal to $\sigma_0/\tau(0)$. The characteristic field in the exponential, 0.013 T, is close to the value obtained when setting $\alpha_e = 1$ in Eq. (1).

Fits of subsets of the data can reveal asymptotic and transitional dependencies on the magnetic field. The inset of Fig. 7b show a $p = \frac{1}{2}$ power-law fit to the data between $B = 0.005$ and $B = 0.050$ T (red line). Also shown is a $p = 1$ power-law fit to the data from $B = 0.011$ to $B = 0.123$ T (green line).

In this experiment we measure the evolution of the ion density distribution. Information regarding the electron temperature and density evolution can only be inferred. Similarly, we can calculate the ion kinetic energy, but not the electron energy or the overall electrical potential energy. The hydrodynamic expansion model used for both $\sigma_{\|}$ and $\sigma_{\perp}$ suggests an anisotropic adiabatic plasma expansion. This model assumes quasi-neutrality, with $n_i \approx n_e$ and a uniform temperature for electrons throughout the plasma. The magnetic field could influence the evolution of the electron temperature and density. Even in the presence of a magnetic field, at time $t = 0$ the electrons begin with an isotropic velocity distribution with an average kinetic energy of $E_e/(3k_B/2) = 96$ K. As the plasma expands, a temperature anisotropy could develop due to adiabatic cooling of the electrons in the parallel direction. The ion expansion, which is what we observe in the experiments, occurs over several microseconds (see Table I), which corresponds to thousands of electron-ion collision times and tens of thousands of electron-electron collision times. Any temperature anisotropy for the weakly coupled electrons, if it exists, will be small [30, 50].

V. COMPARISON TO THEORETICAL MODELS

In this section, we compare the observed self-similar Gaussian density evolution to two popular models. We will show that a diffusion model fails to reproduce the observed time-evolving transverse density profile. We also show that a straightforward implementation of an explicitly self-similar expansion model predicts expansion dynamics at odds from the experimental data.

A. Ambipolar Diffusion model

Ambipolar diffusion is often invoked to model cross-field electron and ion motion in magnetized plasmas [37]. The diffusion equation in the presence of a uniform magnetic field in 1D-cylindrical coordinates is given by

$$\frac{\partial n}{\partial t} = \frac{1}{r}\frac{\partial}{\partial r} r D_{\perp} \frac{\partial n}{\partial r} - F_{\text{loss}}(n,t), \tag{8}$$

where $n(r,t)$ is the radial density distribution of the plasma and F_{loss} represents expansion of the plasma along the magnetic field direction. In Ref. [37] expansion along the magnetic field lines was assumed to follow a self-similar (Gaussian) hydrodynamic model. The loss term assumed the form,

$$F_{\text{loss}}(n,t) = n\frac{t}{\tau^2\left(1 + t^2/\tau^2\right)}, \tag{9}$$

where $\tau = [(m_i\sigma_0^2)/(k_{\text{B}}T_e)]^{1/2}$ is the characteristic expansion time for the plasma.

We solve Eq. (8) numerically. The equation is discretized in space using a second order centered finite difference method, which is numerically integrated using the method of lines [51] with the implicit Runge-Kutta (Radau) method.

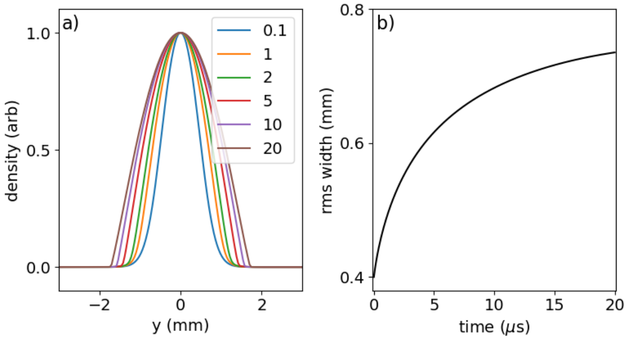

FIG. 8. Numerical solutions for the diffusion equation, Eq. (8), for $B = 0.005$ T, $n_0 = 3\times10^{15}$ cm^{-3}, and $\sigma_0 = 0.4$ mm. a) Scaled plots of the density profile $n(y,t)$. The values of t in μs are indicated in the legend. b) The rms width of the distribution as a function of time. For higher values of B, the expansion proceeds more slowly. However, the fast initial rise followed by a slower rise with a gradually decreasing slope is true for all values of B. This is in opposition to the measured behavior in Fig. 7a and Eq. (3).

The diffusion coefficient appropriate for a wide range of magnetic field strengths is [52]

$$D_{\perp} = D_0 \frac{\nu_{ei}^2}{\nu_{ei}^2 + \Omega_{ce}^2}, \tag{10}$$

where $D_0 = k_B T_e/m_e\nu_{ei}$ is the diffusion coefficient with no magnetic field and ν_{ei} is the electron-ion collision frequency [44]. In the limit $\Omega_{ce} \gg \nu_{ei}$, this diffusion coefficient matches the expression used in [37]. We expect numerical solutions of Eq. (8) to be most appropriate when the plasma is magnetized.

The numerical solutions of $n(r,t)$ are shown in Fig. 8 for $B = 0.005$ T. In panel a) the radial density profile is plotted. Although the profile begins as a Gaussian profile, diffusion flattens the center of the distribution where the density is higher. In the wings of the distribution, where the density drops, diffusion effectively turns off. For higher values of B, the expansion proceeds more slowly.

In Fig. 8b we plot the rms width of the distribution,

$$w_{\text{rms}} = \sqrt{\left(\sum_i y_i^2 n_i\right) / \left(\sum_i n_i\right)}, \tag{11}$$

where the index i runs over the grid points in the calculation, y_i is the spatial grid point and n_i is the density at that grid point. The rms width increases rapidly at first, followed by a slower rise with gradually decreasing slope. This behavior is qualitatively the same for all values of the magnetic field strength. It contradicts the ansatz and conclusion of Ref. 37, the measured behavior in Fig. 7a, and the hydrodynamic model in Eq. (3). If the magnetized UNP expansion was diffusive, plots of $\sigma_{\perp}^2(t)$ would be linear in time (see Fig. 7a).

The failure of the diffusion model for UNPs is not entirely surprising. Ambipolar diffusion is most appropriate in weakly ionized plasmas in which the neutral atoms provide a significant drag force [52]. Furthermore, Eq. (8) does not include ion inertia, which is a dominant feature in UNP expansion. Ultracold neutral plasmas are essentially fully-ionized electron-ion plasmas. The neutral atoms that remain are at such a low density that they have no influence on the expansion dynamics [53].

B. Self similar unmagnetized plasma expansion model

A self-similar plasma expansion model [43, 54] works well for unmagnetized UNPs. The fluid equations of motion for species s can be written,

$$\begin{aligned}\frac{\partial \mathbf{u}_s(\mathbf{r},t)}{\partial t} &= -\mathbf{u}_s(\mathbf{r},t)\cdot\boldsymbol{\nabla}\mathbf{u}_s(\mathbf{r},t)\\ &-\frac{k_B}{m_s n_s(\mathbf{r},t)}\left[T_s(\mathbf{r},t)\boldsymbol{\nabla}n_s(\mathbf{r},t)\right]\\ &+\frac{q_s}{m_s}\left[\mathbf{E}(\mathbf{r},t)+\mathbf{u}_s(\mathbf{r},t)\times\mathbf{B}(\mathbf{r},t)\right] \qquad (12)\end{aligned}$$

where $\mathbf{u}_s$ is the hydrodynamic flow velocity and $\mathbf{E}$ and $\mathbf{B}$ are the electric and magnetic fields. This equation includes advection, pressure, and the Lorentz force.

We first consider a spherically symmetric two component plasma, consisting of only ions ($Z = 1$) and electrons in the absence of a magnetic field. Neglecting the ion pressure term, the equations of motion for the ions and electrons are written

$$\frac{\partial u_i}{\partial t}+u_i\frac{\partial u_i}{\partial r} = -\frac{e}{m_i}\frac{\partial \Phi}{\partial r} \qquad (13)$$

$$\frac{\partial u_e}{\partial t}+u_e\frac{\partial u_e}{\partial r} = \frac{e}{m_e}\frac{\partial \Phi}{\partial r}-\frac{k_B}{m_e n_e}\frac{\partial}{\partial r}(n_e T_e) \qquad (14)$$

where we have rewritten $\mathbf{E} = -\boldsymbol{\nabla}\Phi$ in terms of the potential Φ. In the usual way, multiplying Eq. (14) by m_e and recognizing that the left-hand side of the equation is negligibly small gives an expression for $\partial\Phi/\partial r$, reducing Eq. (13) to,

$$\frac{\partial u_i}{\partial t}+u_i\frac{\partial u_i}{\partial r} = -\frac{k_B}{m_i n_e}\frac{\partial}{\partial r}(n_e T_e). \qquad (15)$$

The electron density on the right-hand side of Eq. (15) is not known exactly. We use the ion density as an approximation of the electron density profile (the so-called quasi-neutral approximation). Further assuming that T_e has a uniform spatial profile, a Gaussian density profile of the form,

$$n(r,t) = n_0\left(\frac{\sigma_0}{\sigma(t)}\right)^3 \exp\left[\frac{-r^2}{2\sigma(t)^2}\right], \qquad (16)$$

is a solution to Eq. (15) [49, 55–57]. In this density profile, $\sigma(t)$ is defined for $B = 0$ in Eq. (3) and n_0 is the plasma density at $r = 0$ and $t = 0$. The self-similar expansion model is plotted against our data in Fig. 5 and Fig. 7a and is a reasonable representation of the unmagnetized data.

C. Self similar magnetized plasma expansion model

In this section we apply the self-similar model to the case of non-zero magnetic field. The system of equations, in cylindrical coordinate, is composed by the continuity equation of each species $s = i, e$

$$\frac{\partial n_s}{\partial t}+\frac{1}{r}\frac{\partial}{\partial r}\left(r n_s u_{r,s}\right)+\frac{\partial}{\partial z}\left(n_s u_{z,s}\right) = 0, \qquad (17)$$

the electron equations of motion,

$$\frac{\partial u_{r,e}}{\partial t}+u_{r,e}\frac{\partial u_{r,e}}{\partial r}-\frac{u_{\theta,e}^2}{r} = -\frac{k_B T_e}{m_e}\frac{1}{n_e}\frac{\partial n_e}{\partial r}+\frac{e}{m_e}\frac{\partial \Phi}{\partial r}-\Omega_{ce}u_{\theta,e}, \qquad (18)$$

$$\frac{\partial u_{\theta,e}}{\partial t}+u_{r,e}\frac{\partial u_{\theta,e}}{\partial r}+\frac{u_{\theta,e}u_{r,e}}{r} = \Omega_{ce}u_{r,e}, \qquad (19)$$

$$\frac{\partial u_{z,e}}{\partial t}+u_{z,e}\frac{\partial u_{z,e}}{\partial z} = -\frac{k_B T_e}{m_e}\frac{1}{n_e}\frac{\partial n_e}{\partial z}+\frac{e}{m_e}\frac{\partial \Phi}{\partial z}, \qquad (20)$$

and the ion equations of motion,

$$\frac{\partial u_{r,i}}{\partial t} + u_{r,i}\frac{\partial u_{r,i}}{\partial r} - \frac{u_{\theta,i}^2}{r} = -\frac{e}{m_i}\frac{\partial \Phi}{\partial r}, \tag{21}$$

$$\frac{\partial u_{\theta,i}}{\partial t} + u_{r,i}\frac{\partial u_{\theta,i}}{\partial r} + \frac{u_{\theta,i}u_{r,i}}{r} = 0, \tag{22}$$

$$\frac{\partial u_{z,i}}{\partial t} + u_{z,i}\frac{\partial u_{z,i}}{\partial z} = -\frac{e}{m_i}\frac{\partial \Phi}{\partial z}. \tag{23}$$

The right hand side of Eq. (19) represents the $\mathbf{E}\times\mathbf{B}$ drift. In writing these equations, we assume that there is no angular dependence in each component of the flow velocities, *i.e.* $u_{\alpha,s}(r,\theta,z,t) = u_{\alpha,s}(r,z,t)$ where $\alpha = r,\theta,z$, no z dependence for the perpendicular components, *i.e.* $u_{\theta,s}(r,z,t) = u_{\theta,s}(r,t)$, $u_{r,s}(r,z,t) = u_{r,s}(r,t)$, and no radial dependence of the $\hat{z}$ velocity component, *i.e.* $u_{z,s}(r,z,t) = u_{z,s}(z,t)$ as indicated by the cylindrical symmetry of the problem. We have also neglected the collision terms because the self-similar model assumes $\mathbf{u}_e = \mathbf{u}_i$. Furthermore, in the ion equation of motion we neglect the cyclotron frequency terms and the ion pressure term.

As with the unmagnetized case, we assume that plasma expansion in the $\hat{z}$ direction is driven by electron pressure alone. This leads to a so-called "collisionless" model in the $\hat{z}$ direction, consistent with previous work [49, 56]. For a self-similar expansion model, this means that the collisions do not modify the distribution functions.

We assume a self-similar ion density expression,

$$n_i(r,z,t) = \frac{n_{0,i}}{\sigma_\perp^2(t)\sigma_\parallel(t)}\exp\left[-\frac{r^2}{\sigma_\perp^2(t)} - \frac{z^2}{\sigma_\parallel^2(t)}\right], \tag{24}$$

with $\sigma_\perp(t) = \sigma_0(1 + t^2/\tau_\perp^2)^{1/2}$ and $\sigma_\parallel(t) = \sigma_0(1 + t^2/\tau_\parallel^2)^{1/2}$, where $\tau_\perp$ and $\tau_\parallel$ are characteristic expansion times in the perpendicular and parallel directions. They can depend on B, but not on t or r. Substituting the above expression in the continuity equation of the ions we obtain

$$\begin{aligned} 2n_i\left[\left(\frac{z^2}{\sigma_\parallel^2} - \frac{1}{2}\right)\frac{1}{\sigma_\parallel}\frac{d\sigma_\parallel}{dt} + \left(\frac{r^2}{\sigma_\perp^2} - 1\right)\frac{1}{\sigma_\perp}\frac{d\sigma_\perp}{dt}\right] \\ + \frac{1}{r}\frac{\partial r n_i u_r}{\partial r} + \frac{\partial n_i u_z}{\partial z} = 0. \end{aligned} \tag{25}$$

Separating the perpendicular and parallel equations we find the following

$$2\left(\frac{z^2}{\sigma_\parallel^2} - \frac{1}{2}\right)\frac{1}{\sigma_\parallel}\frac{d\sigma_\parallel}{dt} - 2\frac{z}{\sigma_\parallel^2}u_{z,i} + \frac{\partial u_{z,i}}{\partial z} = 0, \tag{26}$$

$$2\left(\frac{r^2}{\sigma_\perp^2} - 1\right)\frac{1}{\sigma_\perp}\frac{d\sigma_\perp}{dt} + \frac{u_{r,i}}{r} - 2\frac{r}{\sigma_\perp^2}u_{r,i} + \frac{\partial u_{r,i}}{\partial r} = 0, \tag{27}$$

whose solutions are

$$u_{z,i}(z,t) = \frac{z}{\sigma_\parallel}\frac{d\sigma_\parallel}{dt}, \quad u_{r,i}(r,t) = \frac{r}{\sigma_\perp}\frac{d\sigma_\perp}{dt}. \tag{28}$$

The electric field in Eq. (21) is obtained from the electron equations of motion. The steady state solution of Eq. (19), valid when $t \gg \Omega_{ce}^{-1}$, leads to

$$u_{\theta,e}(r) = \frac{\Omega_{ce} r}{2}. \tag{29}$$

Substituting this into Eq. (18), and neglecting the Burgers' term, $u_{r,e}\partial u_{r,e}/\partial r \approx 0$, leads to an expression for the electric field

$$\frac{\partial \Phi}{\partial r} = \frac{m_e}{e}\frac{\Omega_{ce}^2}{4}r + \frac{k_B T_e}{e}\frac{1}{n_e}\frac{\partial n_e}{\partial r}. \tag{30}$$

For typical experimental conditions, when $B > 0.005$ T, $n_e^{-1}\partial n_i/\partial r \approx -r/\sigma_0^2$, and $T_e = 96$ K, the two terms on the right hand side of Eq. (30) are of the same order of magnitude. When $B = 0$, $\partial\Phi/\partial r$ is negative. For $B > 0.005$ T, it is positive and scales as B^2. Substituting Eq. (30) into Eq. (21) we have

$$\frac{\partial u_{r,i}}{\partial t} + u_{r,i}\frac{\partial u_{r,i}}{\partial r} = -\frac{m_e}{m_i}\left(\frac{\Omega_{ce}^2}{4}\right)r - \frac{c^2}{n_i}\frac{\partial n_i}{\partial r} \tag{31}$$

$$= -\left(\frac{1}{4}\frac{e^2B^2}{m_e m_i}\right)r + 2\frac{c^2}{\sigma_\perp^2}r \tag{32}$$

$$\frac{\partial u_{r,i}}{\partial t} + u_{r,i}\frac{\partial u_{r,i}}{\partial r} = -\left[\frac{\Omega_{ce}\Omega_{ci}}{4} - 2\frac{c^2}{\sigma_\perp^2}\right]r, \tag{33}$$

where $c = \sqrt{k_B T_e/m_i}$ and have used the density distribution from Eq. (24). Finally, by using $u_{r,i} = \frac{r}{\sigma_\perp}\frac{\partial\sigma_\perp}{\partial t}$ from the continuity equation we arrive at

$$\frac{\partial^2\sigma_\perp}{\partial t^2} = -\frac{\Omega_{ce}\Omega_{ci}}{4}\sigma_\perp(t) + 2\frac{k_B T_e}{m_i}\frac{1}{\sigma_\perp(t)} \tag{34}$$

In the above equation, $T_e = T_e(t)$ and is dominated by adiabatic expansion in the parallel direction. The temperature equation is,

$$\begin{aligned} \frac{\partial T_e}{\partial t} + \mathbf{u}_e\cdot\boldsymbol{\nabla}T_e &= -2T_e\boldsymbol{\nabla}\cdot\mathbf{u}_e \\ &= 2\frac{T_e}{n_e}\left[\frac{\partial n_e}{\partial t} + \mathbf{u}_e\cdot\boldsymbol{\nabla}n_e\right]. \end{aligned} \tag{35}$$

Using the self-similar density from Eq. (24) and invoking

TABLE II. Table of assumptions made in each model. For both the self-similar and ambipolar diffusion models, we list the physical quantities represented in the plasma equations, the assumptions made, and the mathematical consequences.

Physics $\mathbf{B} = 0$	Self-similar	Ambipolar Diffusion
Quasi-neutrality	$n_e \approx n_i$	$n_e \approx n_i$
e momentum eqn	$\partial \mathbf{u}_e/\partial t = 0$, $\mathbf{u}_e \cdot \boldsymbol{\nabla} \mathbf{u}_e \approx 0$, $\mathbf{u}_e \approx \mathbf{u}_i$ $\rightarrow \boldsymbol{\nabla} P_e = e n_e \mathbf{E}$	$\partial \mathbf{u}_e/\partial t = 0$ $\mathbf{u}_e \cdot \boldsymbol{\nabla} \mathbf{u}_e \approx 0$, $\mathbf{u}_e \neq \mathbf{u}_i$ $\rightarrow \boldsymbol{\nabla} P_e = e n_e \mathbf{E} + n_e \nu_{ei} (\mathbf{u}_e - \mathbf{u}_i)$
ion momentum eqn	$P_i = 0$, $\mathbf{u}_e \approx \mathbf{u}_i$ $\rightarrow \partial \mathbf{u}_i/\partial t + \mathbf{u}_i \cdot \boldsymbol{\nabla} \mathbf{u}_i = q n_i \mathbf{E}$	$\partial \mathbf{u}_i/\partial t = 0$ $\mathbf{u}_e \cdot \boldsymbol{\nabla} \mathbf{u}_i \approx 0$, $\mathbf{u}_e \neq \mathbf{u}_i$ $\rightarrow \boldsymbol{\nabla} P_i = q n_i \mathbf{E} + n_e \nu_{ie} (\mathbf{u}_i - \mathbf{u}_e)$
e pressure	adiab: $P_e(\mathbf{r}, t) = n_e(\mathbf{r}, t) k_B T_e(t)$ isotherm: $P_e(\mathbf{r}, t) = n_e(\mathbf{r}, t) k_B T_e$	no adiabatic isotherm: $P_e(\mathbf{r}) = n_e(\mathbf{r}, t) k_B T_e$
ion pressure	$P_i = 0$	isotherm: $P_i = n_i k_B T_i$

an isothermal approximation ($\boldsymbol{\nabla} T_e = 0$) gives,

$$\begin{aligned} \frac{1}{T_e}\frac{dT_e}{dt} &= 2\frac{1}{n_e}\left[\frac{\partial n_e}{\partial t} + \mathbf{u}_e \cdot \boldsymbol{\nabla} n_e\right] \\ &= \left(\frac{4z^2}{\sigma_\parallel^2} - 2\right)\frac{1}{\sigma_\parallel}\frac{d\sigma_\parallel}{dt} - 4\frac{z}{\sigma_\parallel^2}u_z \\ &= -2\frac{1}{\sigma_\parallel}\frac{d\sigma_\parallel}{dt} \end{aligned} \tag{36}$$

The solution to this equation is,

$$T_e = T_{e0}\left(\frac{\sigma_0}{\sigma_\parallel}\right)^2. \tag{37}$$

Substituting this into Eq. (34) gives,

$$\frac{d^2\sigma_\parallel}{dt^2} = \frac{2c_0^2\sigma_0^2}{\sigma_\parallel^3} \tag{38}$$

$$\frac{d^2\sigma_\perp}{dt^2} = -\frac{\Omega_{ce}\Omega_{ci}\sigma_\perp}{4} + \frac{2c_0^2}{\sigma_\perp}\frac{\sigma_0^2}{\sigma_\parallel^2}, \tag{39}$$

where $c_0 = \sqrt{k_B T_{e0}/m_i}$. As the magnetic field strength increases, the left-hand side of Eq. (39) tends toward zero. In this limit,

$$\sigma_\perp(t) = \frac{c_0\sigma_0}{\sigma_\parallel(t)\, eB}\sqrt{8m_i m_e}. \tag{40}$$

Making the time-dependence explicit, Eq. (3), and taking the late time limit, we find

$$\sigma_\perp(t) = \frac{c_0^2}{eB\sigma_0}\sqrt{8m_e m_i}\; t, \tag{41}$$

$$\equiv v_{\text{exp}} t \tag{42}$$

In the inset to Fig. 7b, the power-law fit with $p = 1$ gives

$$v_{\text{exp}} = \frac{0.04 \pm 0.01\ \text{T} \cdot \text{m/s}}{B - (0.003 \pm 0.002\ \text{T})}, \tag{43}$$

where the uncertainties indicate the estimated statistical errorbars in the fit parameters. The prediction of Eq. (42) is

$$v_{\text{exp}} \sim \frac{0.2\ \text{T} \cdot \text{m/s}}{B}, \tag{44}$$

about a factor of 5 faster than the model prediction. Also of concern is that the small-B solution of Eq. (39) is unphysical because it predicts that $\sigma_\perp$ oscillates in time.

VI. DISCUSSION

In this paper we present measurements of UNP expansion in a strong magnetic field. We show that the cross-field expansion, $\sigma_\perp$, is self-similar and Gaussian. This agrees with results reported in Ref. [37]. The present work extends that of Ref. [37] by probing much stronger fields, specifically 17× stronger.

We show that plasma expansion along the magnetic field lines is Gaussian and self-similar. The present results are limited to measurements near the center of the plasma in the parallel direction.

Our experimental results are compared to two theoretical models. Both models predict behavior that does not match the experimental results. We show that ambipolar diffusion does not produce a self-similar expansion. Although this model was invoked in Ref. [37], it is inappropriate for UNPs. The diffusion model assumes that electron and ion motion is strongly damped by collisions with neutral atoms, a condition that is not met for UNPs.

We extend an explicitly self-similar expansion model to include a uniform magnetic field. We explicitly retained the time-dependent momentum equation, something that is missing in the diffusion equation (see Table II). The ion equations of motion are therefore second-order in time, making wavelike solutions possible. In the large B limit, this model predicts that the asymptotic expansion velocity scales as B^{-1}, although with a larger prefactor than the experiment suggests. At smaller values of B this model predicts that $\sigma_\perp(t)$ is an oscillating function of time.

These UNP results demonstrate that simple self-similar models can only predict limited aspects of the plasma expansion physics. The disagreement between the models and the experimental results call the approximations and essential physics of the models into question. Future theoretical and computational work is clearly needed in this area. The present work suggests that the lowest-order simple models fail to capture the essential physics of magnetized plasma expansion. The next simplest approach requires a numerical magneto-hydrodynamic or kinetic theory solution. Future experimental work could measure spatially-resolved ion temperature and density. The present work uses a large diameter probe laser beam, averaging the plasma density in the x direction. It may be that spatially resolved temperature and density measurements could provide more insight into the plasma expansion dynamics, hydrodynamic velocity field, and collision energetics. Future work could also probe a wider range of density and initial electron temperature to more fully map the parameter space.

VII. ACKNOWLEDGMENTS

We would like to thank Dr. Ross Spencer for useful conversation. R.T.S. and S.D.B. acknowledge support from the U.S. Air Force Office of Scientific Research Grant No. FA9550-17-1-0302 and the National Science Foundation Grant No. PHY-2009999. M.S.M. and L.G.S. were supported by the U.S. Air Force Office of Scientific Research Grant No. FA9550-17-1-0394.

[1] E. V. Crockett, R. C. Newell, F. Robicheaux, and D. A. Tate, Phys. Rev. A **98**, 043431 (2018).

[2] S. D. Bergeson, S. D. Baalrud, C. L. Ellison, E. Grant, F. R. Graziani, T. C. Killian, M. S. Murillo, J. L. Roberts, and L. G. Stanton, Physics of Plasmas **26**, 100501 (2019).

[3] T. K. Langin, G. M. Gorman, and T. C. Killian, Science **363**, 61 (2019).

[4] M. A. Viray, S. A. Miller, and G. Raithel, Phys. Rev. A **102**, 033303 (2020).

[5] T. Kroker, M. Großmann, K. Sengstock, M. Drescher, P. Wessels-Staarmann, and J. Simonet, Nature Communications **12** (2021), 10.1038/s41467-020-20815-8.

[6] P. McQuillen, T. Strickler, T. Langin, and T. C. Killian, Physics of Plasmas **22**, 033513 (2015).

[7] G. Bannasch, J. Castro, P. McQuillen, T. Pohl, and T. C. Killian, Phys. Rev. Lett. **109**, 185008 (2012).

[8] T. S. Strickler, T. K. Langin, P. McQuillen, J. Daligault, and T. C. Killian, Phys. Rev. X **6**, 021021 (2016).

[9] T. Sprenkle, A. Dodson, Q. McKnight, R. Spencer, S. Bergeson, A. Diaw, and M. S. Murillo, Phys. Rev. E **99**, 053206 (2019).

[10] W.-T. Chen, C. Witte, and J. L. Roberts, Phys. Rev. E **96**, 013203 (2017).

[11] P. Jiang and J. L. Roberts, Physics of Plasmas **26**, 043513 (2019).

[12] M. Aghigh, K. Grant, R. Haenel, K. L. Marroquín, F. B. V. Martins, H. Sadegi, M. Schulz-Weiling, J. Sous, R. Wang, J. S. Keller, and E. R. Grant, Journal of Physics B: Atomic, Molecular and Optical Physics **53**, 074003 (2020).

[13] J. Sous and E. Grant, Phys. Rev. Lett. **120**, 110601 (2018).

[14] R. T. Farouki and S. Hamaguchi, The Journal of Chemical Physics **101**, 9885 (1994), https://doi.org/10.1063/1.467955.

[15] M. Baus and J.-P. Hansen, Physics Reports **59**, 1 (1980).

[16] L. G. Stanton, J. N. Glosli, and M. S. Murillo, Phys. Rev. X **8**, 021044 (2018).

[17] L. G. Stanton and M. S. Murillo, Phys. Rev. E **93**, 043203 (2016).

[18] S. D. Baalrud and J. Daligault, Phys. Rev. Lett. **110**, 235001 (2013).

[19] T. M. Wilson, W.-T. Chen, and J. L. Roberts, Phys. Rev. A **87**, 013410 (2013).

[20] J. P. Morrison, C. J. Rennick, J. S. Keller, and E. R. Grant, Phys. Rev. Lett. **101**, 205005 (2008).

[21] P. Arnold, G. D. Moore, and L. G. Yaffe, Journal of High Energy Physics **2000**, 001 (2000).

[22] Z. Donkó and P. Hartmann, Phys. Rev. E **78**, 026408 (2008).

[23] J. Clérouin, P. Arnault, B.-J. Gréa, S. Guisset, M. Vandenboomgaerde, A. J. White, L. A. Collins, J. D. Kress, and C. Ticknor, Phys. Rev. E **101**, 033207 (2020).

[24] L. G. Silvestri, R. T. Sprenkle, S. D. Bergeson, and M. M. Murillo, Physics of Plasmas **28**, 062302 (2021).

[25] R. T. Sprenkle, L. G. Silvestri, M. S. Murillo, and S. D. Bergeson, Nature Communications **13** (2022), 10.1038/s41467-021-27696-5.

[26] T. Ott, H. Löwen, and M. Bonitz, Phys. Rev. E **89**, 013105 (2014).

[27] T. Ott and M. Bonitz, Phys. Rev. Lett. **107**, 135003 (2011).

[28] T. Ott, H. Kählert, A. Reynolds, and M. Bonitz, Phys. Rev. Lett. **108**, 255002 (2012).

[29] M. R. Gomez, S. A. Slutz, A. B. Sefkow, D. B. Sinars, K. D. Hahn, S. B. Hansen, E. C. Harding, P. F. Knapp, P. F. Schmit, C. A. Jennings, T. J. Awe, M. Geissel, D. C. Rovang, G. A. Chandler, G. W. Cooper, M. E. Cuneo, A. J. Harvey-Thompson, M. C. Herrmann, M. H. Hess, O. Johns, D. C. Lamppa, M. R. Martin, R. D. McBride, K. J. Peterson, J. L. Porter, G. K. Robertson, G. A. Rochau, C. L. Ruiz, M. E. Savage, I. C. Smith, W. A. Stygar, and R. A. Vesey, Phys. Rev. Lett. **113**, 155003 (2014).

[30] S. D. Baalrud and J. Daligault, Phys. Rev. E **96**, 043202 (2017).

[31] F. Boeschoten, Journal of Nuclear Energy. Part C, Plasma Physics, Accelerators, Thermonuclear Research **6**, 339 (1964).

[32] F. C. Hoh, Rev. Mod. Phys. **34**, 267 (1962).

[33] S. S. Harilal, M. S. Tillack, B. O'Shay, C. V. Bindhu, and F. Najmabadi, Phys. Rev. E **69**, 026413 (2004).

[34] G. Serianni, M. Agostini, V. Antoni, R. Cavazzana, E. Martines, F. Sattin, P. Scarin, E. Spada, M. Spolaore, N. Vianello, and M. Zuin, Plasma Physics and Controlled Fusion **49**, B267 (2007).

[35] J. M. Guthrie and J. L. Roberts, Physics of Plasmas **28**, 052101 (2021), https://doi.org/10.1063/5.0047640.

[36] T. Ott, M. Bonitz, and Z. Donkó, Phys. Rev. E **92**, 063105 (2015).

[37] X. L. Zhang, R. S. Fletcher, S. L. Rolston, P. N. Guzdar, and M. Swisdak, Phys. Rev. Lett. **100**, 235002 (2008).

[38] S. K. Tiwari and S. D. Baalrud, Physics of Plasmas **25**, 013511 (2018), https://doi.org/10.1063/1.5013320.

[39] B. Scheiner and S. D. Baalrud, Phys. Rev. E **102**, 063202 (2020).

[40] T. Lafleur and S. Baalrud, Plasma Physics and Controlled Fusion **62** (2020), https://doi.org/10.1088/1361-6587/ab9bea.

[41] S. D. Baalrud and J. Daligault, Contributions to Plasma Physics **57**, 238 (2017).

[42] G. M. Gorman, M. K. Warrens, S. J. Bradshaw, and T. C. Killian, Phys. Rev. Lett. **126**, 085002 (2021).

[43] P. Mora, Physics of Plasmas **12**, 112102 (2005), https://doi.org/10.1063/1.2134768.

[44] A. S. Richardson, *2019 NRL Plasma Formulary*, Tech. Rep. (US Naval Research Laboratory, 2019).

[45] D. O. Gericke, M. S. Murillo, and M. Schlanges, Phys. Rev. E **65**, 036418 (2002).

[46] G. Tommaseo, T. Pfeil, G. Revalde, G. Werth, P. Indelicato, and J. P. Desclaux, The European Physical Journal D - Atomic, Molecular and Optical Physics **25**, 113 (2003).

[47] M. Chwalla, J. Benhelm, K. Kim, G. Kirchmair, T. Monz, M. Riebe, P. Schindler, A. S. Villar, W. Hänsel, C. F. Roos, R. Blatt, M. Abgrall, G. Santarelli, G. D. Rovera, and P. Laurent, Phys. Rev. Lett. **102**, 023002 (2009).

[48] B. K. Sahoo and P. Kumar, Phys. Rev. A **96**, 012511 (2017).

[49] S. Laha, P. Gupta, C. E. Simien, H. Gao, J. Castro, T. Pohl, and T. C. Killian, Phys. Rev. Lett. **99**, 155001 (2007).

[50] T. Ott, M. Bonitz, P. Hartmann, and Z. Donkó, Phys. Rev. E **95**, 013209 (2017).

[51] R. J. LeVeque, *Finite difference methods for ordinary and partial differential equations: steady-state and time-dependent problems* (SIAM, 2007).

[52] J. A. Bittencourt, *Fundamentals of plasma physics* (Springer Science & Business Media, 2004).

[53] T. C. Killian, S. Kulin, S. D. Bergeson, L. A. Orozco, C. Orzel, and S. L. Rolston, Phys. Rev. Lett. **83**, 4776 (1999).

[54] P. Mora, Phys. Rev. Lett. **90**, 185002 (2003).

[55] F. Robicheaux and J. D. Hanson, Phys. Rev. Lett. **88**, 055002 (2002).

[56] F. Robicheaux and J. D. Hanson, Physics of Plasmas **10**, 2217 (2003).

[57] S. G. Kuzmin and T. M. O'Neil, Physics of Plasmas **9**, 3743 (2002).

[58] In a binary collision approximation, the argument of the Coulomb logarithm, $\ln\Lambda = \ln(\lambda_D/r_e)$, is the ratio of the largest collision length to the smallest collision length. In this sense, setting $\ell = \lambda_D$ might be justified.

[59] N. V. Kabadi, R. Simpson, P. J. Adrian, A. Bose, J. A. Frenje, M. Gatu Johnson, B. Lahmann, C. K. Li, C. E. Parker, F. H. Séguin, G. D. Sutcliffe, R. D. Petrasso, S. Atzeni, J. Eriksson, C. Forrest, S. Fess, V. Y. Glebov, R. Janezic, O. M. Mannion, H. G. Rinderknecht, M. J. Rosenberg, C. Stoeckl, G. Kagan, M. Hoppe, R. Luo, M. Schoff, C. Shuldberg, H. W. Sio, J. Sanchez, L. B. Hopkins, D. Schlossberg, K. Hahn, and C. Yeamans, Phys. Rev. E **104**, L013201 (2021).

[60] R. Sprenkle, L. Silvestri, M. S. Murillo, and S. Bergeson, Research Square (2021), 10.21203/rs.3.rs-159714/v1.

[61] S. V. Lebedev, L. Suttle, G. F. Swadling, M. Bennett, S. N. Bland, G. C. Burdiak, D. Burgess, J. P. Chittenden, A. Ciardi, A. Clemens, P. de Grouchy, G. N. Hall, J. D. Hare, N. Kalmoni, N. Niasse, S. Patankar, L. Sheng, R. A. Smith, F. Suzuki-Vidal, J. Yuan, A. Frank, E. G. Blackman, and R. P. Drake, Physics of Plasmas **21**, 056305 (2014), https://doi.org/10.1063/1.4874334.

[62] K. Matsuo, H. Nagatomo, Z. Zhang, P. Nicolai, T. Sano, S. Sakata, S. Kojima, S. H. Lee, K. F. F. Law, Y. Arikawa, Y. Sakawa, T. Morita, Y. Kuramitsu, S. Fujioka, and H. Azechi, Phys. Rev. E **95**, 053204 (2017).

[63] L. B. Fletcher, A. L. Kritcher, A. Pak, T. Ma, T. Döppner, C. Fortmann, L. Divol, O. S. Jones, O. L. Landen, H. A. Scott, J. Vorberger, D. A. Chapman, D. O. Gericke, B. A. Mattern, G. T. Seidler, G. Gregori, R. W. Falcone, and S. H. Glenzer, Phys. Rev. Lett. **112**, 145004 (2014).

[64] Y. Zhou, T. T. Clark, D. S. Clark, S. G. Glendinning, M. A. Skinner, C. M. Huntington, O. A. Hurricane, A. M. Dimits, and B. A. Remington, Physics of Plasmas **26**, 080901 (2019).

[65] Y. Zhou, Physics Reports **723-725**, 1 (2017).

[66] J. B. Taylor, Physics of Fluids **14**, 1492 (1971).

[67] C. Ticknor, J. D. Kress, L. A. Collins, J. Clérouin, P. Arnault, and A. Decoster, Phys. Rev. E **93**, 063208 (2016).